PAPER

Check for updates

Synergistically self-assembled *in situ* growth of MXene@MOF derived sodium alginate hydrogel 3D frameworks as next-generation electrocatalysts for oxygen and hydrogen evolution†

Saleem Raza, [ID] ‡[a] Ata Ur Rehman, [ID] ‡[ac] Cheng Chen,[ab] Tianyu Zhao, [ID] [d] Asif Hayat,[a] Tariq Bashir,[a] Liguo Shen, [ID] *[ab] Yasin Orooji [ID] *[a] and Hongjun Lin [ID] *[a]

The need to minimize carbon emissions and improve sustainable energy systems has stimulated significant research into multifunctional materials. This work presents a unique MXene@MOF and sodium alginate hydrogel composite as an electrocatalyst in energy storage and conversion. The Max-phase titanium niobium aluminum carbide (TiNbAlC) was etched to remove Al layers, producing MXene (TiNbCTx). The MXene nanosheets were dispersed in methanol, ultrasonicated, and mixed with polyvinylpyrrolidone (PVP). Subsequently, $Zn(NO_3)_2 \cdot 6H_2O$ and $Co(NO_3)_2 \cdot 6H_2O$ were added, followed by 2-methylimidazole, and stirred for 2 h. After 4 h, centrifugation, washing, and freeze-drying produced TiNbC@MOF. This composite was further incorporated into a sodium alginate hydrogel to construct TiNbC/MOF@SA-H. Besides, the characterization included SEM, EDX, XRD, FTIR, AFM, TGA, and XPS analysis. The performance of the electrocatalyst was assessed for the oxygen evolution reaction (OER) and hydrogen evolution reaction (HER) in an alkaline medium (1 M KOH). TiNbC/MOF@SA-H demonstrated excellent capacitance, high rate capability, and stability over 1000 cycles. TiNbC/MOF@SA-H demonstrates enhanced OER electrocatalytic performance relative to the reference IrO_2 and the composite TiNbC/MOF, exhibiting low overpotentials of 185, 188 and 204 mV at current densities of 10, 20 and 50 mA cm^{-2}, respectively. Additionally, it shows superior HER catalytic activity compared to other prepared samples, requiring only 17, 79 and 325 mV to achieve current densities of 10, 50 and 100 mA cm^{-2}, respectively. The material achieved an OER Tafel slope of 84 mV dec^{-1} and a HER Tafel slope of 61.8 mV dec^{-1} at a 1 V s^{-1} scan rate.

1. Introduction

As Earth's resources are being quickly mined and consumed, the problems of environmental degradation and shortages of energy are becoming increasingly severe. Hence, there is an immediate need to advance environmentally friendly, sustainable, and unpolluted energy sources in contemporary civilization.[1,2] The increasing need for effective and intelligent solutions for energy storage, preservation, and usage is driven by the necessity for sustainable clean energy.[3,4] Electrochemical energy storage and conversion technologies are crucial for stabilizing the power supply from renewable sources. Renewable energy sources, including solar, wind, and wave, often provide electricity intermittently owing to fluctuating environmental circumstances. These technologies enable the storage of surplus energy during periods of high production and its subsequent release during periods of low output, thereby ensuring a stable and dependable energy supply.[5,6] Batteries and capacitors are well recognized as electrochemical energy storage and conversion devices that are now being used commercially in modern civilization[5,7] Furthermore, the hydrogen and oxygen evolution reactions (HER and OER) represent a novel type of electrochemical energy conversion process, characterized by both high capacitance and the ability to deliver high-power energy outputs.[8,9] It is considered a developing electrochemical energy storage technology that complements existing battery and capacitor technologies, providing new opportunities for efficient energy production.[10,11]

In recent years, considerable research has been conducted to investigate the properties and potential applications of 2D

[a]*College of Geography and Environmental Sciences, Zhejiang Normal University, Jinhua, 321004, P. R. China. E-mail: lgshen@zjnu.cn; hjlin@zjnu.cn*

[b]*Henan Key Laboratory of Water Pollution Control and Rehabilitation Technology, Henan University of Urban Construction, Pingdingshan, 467036, China*

[c]*Key Laboratory of the Ministry of Education for Advanced Catalysis Materials, Institute of Physical Chemistry, Zhejiang Normal University, Jinhua 321004, China*

[d]*School of Chemical Engineering, Northwest University, Xian, Shaanxi 710069, China*

‡ These two authors contributed equally.

MXene structures, which have shown promising abilities in the areas of energy conversion, batteries, pollutant removal and energy storage.[12,13] MXene structures are often produced by synthesizing Max-phases utilizing several techniques, including aluminum layer etching with fluoride salts, chloride-based procedures, aqueous electrolytes, molten salts in air, electrochemical methods, and hydrogen fluoride (HF) treatments.[14,15] The accordion-like structures of MXenes have been thoroughly researched due to their significant catalytic effects and functional roles in enhancing material performance.[16] Conversely, MXenes are among the latest 2D nanosheets that have garnered considerable attention.[17] MXenes have been employed across various fields, including photocatalysis, supercapacitors, the oxygen evolution reaction (OER), the hydrogen evolution reactions (HER), membrane technologies, *etc.*[18,19] These nanosheets are highly valued for their extensive surface area, exceptional dispersibility, outstanding mechanical stability, and remarkable thermal and electrical conductivity.[20] MXenes encompass various categories and types; TiNbCTx is a recently synthesized variant that has quickly gained attention from researchers.[21] Nevertheless, the significant swelling and limited resistance to oxidation of MXene in water render it vulnerable to aqueous environments and harmful adsorption.[22] Randomly arranged nanosheets emphasize the need for modification to facilitate the industrial applications of these materials.[23] The energy storage and conversion characteristics of bimetallic Ti/Nb carbides can significantly enhance kinetic rates, thermodynamic efficiency, and cycling stability in hydrogel applications, particularly benefiting supercapacitor technology through increased surface exposure.[24,25] The incorporation of multiple interface regions involving TiNbC@MOF and hydrogels, particularly utilizing bimetallic MXene, could potentially boost HER and OER performance beyond what a simple hydrogel could achieve.

Metal–organic frameworks (MOFs) are a category of nanomaterials distinguished by their distinctive structure, consisting of metal ions or clusters interconnected by organic ligands. This distinct arrangement allows MOFs to have high surface areas and tunable porosity, making them highly useful in applications such as gas storage, separation, and catalysis. These materials form porous networks with well-defined structures that can exhibit a range of properties based on the choice of metals and organic linkers used in their synthesis.[26,27] Nowadays, MOFs are widely utilized due to their numerous advantages, which include diverse morphologies such as 2D lamellar structures, polyhedrons, microns, and nano-sized particles.[28,29] Furthermore, MOFs exhibit a large specific surface area, strong affinity for water, and adjustable functionality.[30] Hence, MOFs are considered ideal candidates for fabricating materials with specific functionalities, exemplified by ultra-high porosity and amine groups that make them suitable for *in situ* growth on compatible supports.[31] Moreover, synthesizing these particles does not necessitate challenging conditions or a complex environment. However, due to their inorganic nature, MOFs have faced challenges in dispersion within organic phases, resulting in low stability for long-term applications to this day.[32,33] Research in MXenes and MOFs

for the HER and OER has advanced significantly and continues to rapidly expand, with thousands of papers published annually on the subject.[34,35] This underscores the importance of investigating MXenes and MOFs, with an expectation for continued growth in hybrids like TiNbC@MOFs.

Moreover, polymer-infused hydrogels exhibit unique characteristics and are extensively used in the fabrication of battery components, energy solutions, and drug delivery, adsorption and release mechanisms, among several other applications.[36–38] While natural polymer hydrogels offer numerous advantages, they often do not meet the required performance standards for certain applications.[39] As a result, several technological advancements have been developed to optimize the production process of hydrogels, thereby enhancing their fundamental properties.[40] In recent developments, incorporating MXene and MOF materials into hydrogel networks has proven highly effective in enhancing their performance characteristics, especially in fields like energy storage and conversion. This approach leverages the unique properties of MXene and MOFs, such as high conductivity and large surface area, to significantly improve the functionality and efficiency of hydrogels used in various technological applications. This synergy allows for advancements in areas such as battery components, supercapacitors, and HER and OER catalytic systems, where the combined properties of hydrogels with MXene and MOF materials offer superior performance compared to traditional hydrogel systems.[41,42] Physical and chemical crosslinking are the fundamental methods used to form the hydrogel network. Physical crosslinking refers to the formation of molecular linkages by non-covalent interactions, including van der Waals forces, hydrogen bonds, electrostatic interactions, and other similar interactions.[43] Hydrogels generated by physical crosslinking exhibit the property of reversibility. However, their mechanical properties are typically inferior and they tend to degrade with use, limiting their potential applications.[44] Chemically crosslinked hydrogels possess robust mechanical strength and have great potential for many applications in the area of polymer hydrogel production.[45,46] The effectiveness and suitability of hydrogels depend on the specific type of chemical reaction and the precise conditions under which it occurs.[47] A novel composite material integrating MXenes, MOFs, and polymer hydrogels was developed to leverage the synergistic properties of these components. The composites exhibit a synergistic interaction between MXene nanosheets and MOFs, while MOFs are incorporated between MXene nanosheets to prevent their restacking, thereby improving stability and optimizing performance across a wide range of applications. The combination of TiNbC@MOF composites with hydrogels produces hybrid materials that show great promise in the fields of energy storage, catalysis, sensing, and electromagnetic wave absorption.[48] This field is experiencing rapid growth, with the number of publications expected to double annually as the relevant literature expands.[49,50]

Herein, low-cost, environmentally friendly MXene, MOF and sodium alginate hydrogels were prepared as follows: we produced TiNbCTx MXene nanosheets by an *in situ* technique using LiF and HCl. These nanosheets were then treated in an

This journal is © The Royal Society of Chemistry 2025

J. Mater. Chem. A, 2025, **13**, 4390–4403 | **4391**

alkaline solution. Finally, we used the TiNbCTx MXene layers as a scaffold for the *in situ* development of functionalized MOF particles utilizing the self-assembly method. After this step, sodium alginate polymers were introduced into TiNbC@MOF to prepare synergistic hydrogels subsequently. The synthesized materials were characterized by using various characterization techniques for their final morphology. The TiNbC@MOF/SA-H composite exhibits exceptional performance in terms of the permeation rate and HER and OER ratio, making it very promising for energy applications.

2. Materials and methods

2.1. Materials

The MAX phase (TiNbAlC) material was obtained from Beijing Beike 2D Materials Co., Ltd and Sinopharm Chemical Reagent Co., Ltd. Additionally, methanol, polyvinyl pyrrolidone (PVP), zinc nitrate hexahydrate ($Zn(NO_3)_2 \cdot 6H_2O$), cobalt nitrate hexahydrate ($Co(NO_3)_2 \cdot 6H_2O$), and 2-methylimidazole were supplied by Shanghai Aladdin Biochemical Technology Co., Ltd. Acetic acid powder, sodium alginate (SA), glutaraldehyde (GA), lithium fluoride (LiF), and anhydrous calcium chloride ($CaCl_2$) were all obtained from Sinopharm Chemical Reagent Co., Ltd, China. In addition, solutions of NaOH and HCl with a concentration of 0.1 mol L^{-1} were made and utilized to modify the pH of the solutions. All deionized water used in the experiments was supplied by a Millipore-Q system. Potassium hydroxide (KOH, 99.9%) was purchased from Sinopharm Chemical Reagent Co., Ltd, China. The carbon paper and zinc plates used as accessories for Zn–air batteries were acquired from Shanghai Hesen Electrical Co., Ltd, located in China.

2.2. Exfoliation of the MAX phase to MXene

This step included dissolving a 2 g sample of titanium niobium aluminum carbide (TiNbAlC) MAX phase, which had a purity of 99%, in a 40 mL solution. This solution consisted of 1.5 g of LiF, HCl, and DI water in a 10 : 30 v/v ratio. The purpose of this step was to remove the aluminum layers. The solution was agitated for 48 h at a temperature of 45 °C, maintaining a consistent rotational speed of 350 rpm.[51] The combination underwent many rounds of centrifugation to maintain a pH range of 6–7, followed by freeze drying for a duration of 12 h. The product was designated as multilayer MXene, specifically identified as TiNbCTx. Subsequently, the sediments were disseminated again in anhydrous ethanol and kept at a low temperature.[52]

2.3. Preparation of MXene@MOF

According to a previously reported method,[53,54] a 40 mg sample of MXene nanosheets was dispersed in 40 mL of methanol and ultrasonicated for 30 min. Then, 40 mg of PVP was added to the solution and stirred for 50 min. Following this, 59.4 mg of zinc nitrate ($Zn(NO_3)_2 \cdot 6H_2O$) and 58.2 mg of cobalt nitrate ($Co(NO_3)_2 \cdot 6H_2O$) were dissolved in the resulting mixture. The mixture was then agitated for a duration of 40 min, followed by a sonication process lasting 20 min. Finally, 20 mL of methanol containing 96.6 mg of 2-methylimidazole was quickly added to

the mixture and stirred for 2 h at room temperature. After sufficient stirring, the mixed solution was aged for 4 h, followed by centrifugation, washing, and freeze-drying treatment for 48 h to obtain TiNbC@MOF.

2.4. Mixing of the TiNbC@MOF sodium alginate hydrogel (TiNbC@MOF/SA@H)
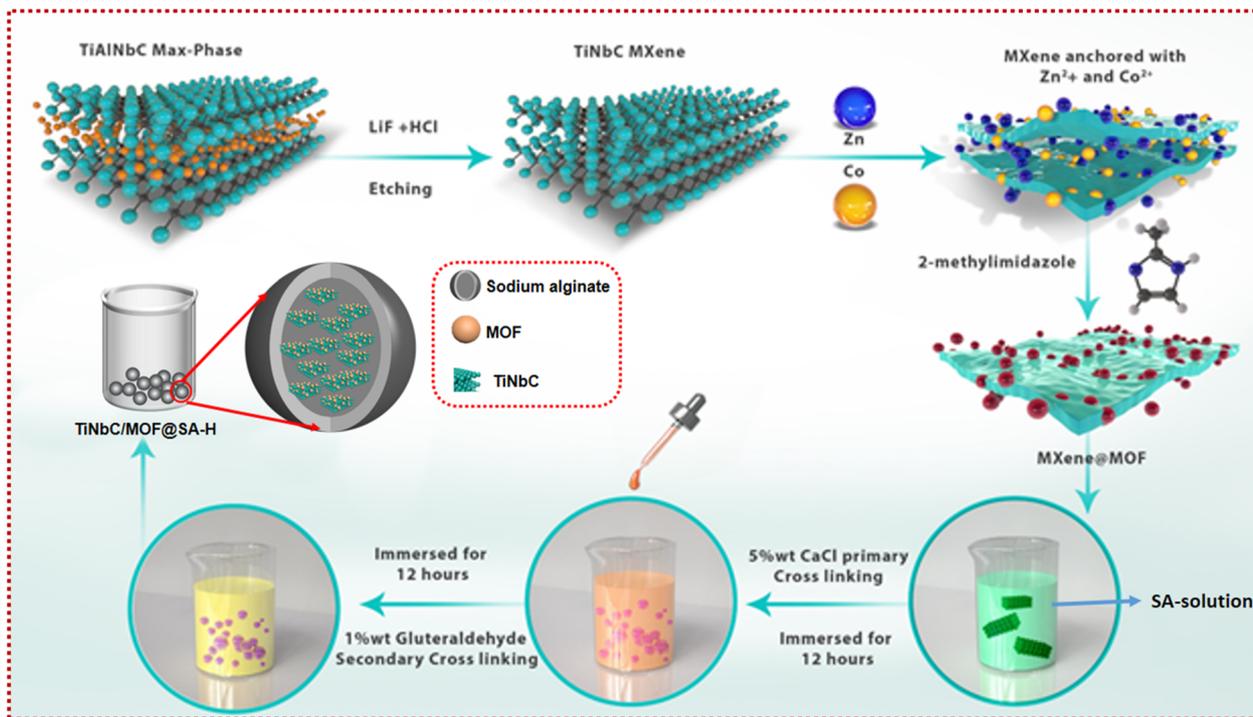
The TiNbC@MOF sodium alginate hydrogel (TiNbC@MOF/SA@H) was produced by chemically crosslinking the solution with $CaCl_2$ as the main crosslinking agent, while glutaraldehyde (GA) served as the secondary crosslinking agent. The SA solution was prepared by dissolving 3.0 g of SA powder in 97.0 g of water, resulting in a 3% weight concentration. This solution was then heated to 90 °C for 24 h to ensure even suspension and expansion. Subsequently, a solution of SA (49.10 g) was added to a beaker containing 0.40 g of TiNbC@MOF materials and stirred. Stirring was continued for at least 2 h to ensure a uniform suspension. The principal crosslinking solution, including 5% $CaCl_2$, was prepared by dissolving 13.58 g of $CaCl_2$ powder in 250 mL of water. The solution's pH was modified to 4 using NaOH (0.1 M) and HCl (0.1 M). Furthermore, the secondary crosslinking solution was formulated by dissolving 2 mL of GA in 98 mL of distilled water.[36,55]

2.5. TiNbC@MOF/SA@H hydrogel 3D framework preparation

According to the previously reported literature,[55] to regulate the feed flow rate to 10 mL h^{-1}, a blend of TiNbC/MOF@SA-H (40 wt%) was dispersed using ultrasound. The mixture was loaded into a 3.0 mm diameter needle injector. The syringe containing the mixture was placed horizontally in a syringe pump. Following this, droplets of the amalgam were injected into the primary crosslinking solution using a syringe injection pump. During the process, the distance between the needle apex and the primary crosslinking emulsion surface was constantly maintained at 8.0 cm. Thereafter, the hydrogel capsules, in their initial form, were submerged in the main crosslinking solution for at least 24 h. The aim of this approach was to enhance the stiffness, malleability, and overall durability of the resulting TiNbC/MOF@SA-H composite. Additionally, a secondary crosslinking solution was used to enhance the stability and mechanical characteristics of the outer surface. Afterwards, the TiNbC/MOF@SA-H hydrogel that developed was separated and extensively cleansed using deionized water. This rinse procedure was repeated more than five times, as shown in Scheme 1. Finally, the produced hydrogel capsules were freeze dried in order to improve the electrochemical properties.

2.6. Characterization

The structural morphology of TiNbC/MOF and its composite with a sodium alginate hydrogel (TiNbC/MOF@SA-H) was analyzed using a scanning electron microscope (SEM) device (Hitachi S-4800). The KBr pellet samples were analyzed for FT-IR spectra using a Nicolet NEXUS 870 infrared spectrometer. X-ray diffraction (XRD), energy-dispersive X-ray spectroscopy (EDX), atomic force microscopy (AFM), thermogravimetric analysis

4392 | *J. Mater. Chem. A*, 2025, **13**, 4390–4403

This journal is © The Royal Society of Chemistry 2025

Scheme 1 Schematic design and preparation of the TiNbC/MOF@SA-H polymer hydrogel for enhanced electrocatalytic activities. This material combines TiNbC with a MOF and SA hydrogel (SA-H). The integration of these components constructs a composite hydrogel with improved electrocatalytic properties. The preparation involves dispersing TiNbC and the MOF into the SA-H matrix, forming a stable and efficient electrocatalytic material. This composite shows promise for applications in energy conversion and storage due to its superior electrochemical performance.

(TGA), and X-ray photoelectron spectroscopy (XPS) analyses were conducted using the equipment available in the laboratory at Zhejiang Normal University.

2.7. Electrochemical study

The electrochemical properties of TiNbC/MOF and TiNbC/MOF@SA-H hydrogels were assessed using a three-electrode setup. Measurements were conducted using a Gamry electrochemical workstation, where a saturated Hg/HgO electrode served as the reference electrode and a carbon rod acted as the counter electrode. To prepare the electrochemical ink for OER activity testing, a catalyst called TiNbC/MOF@SA-H, weighing 5 mg, was combined with 50 μL of Nafion solution with a concentration of 5 wt% and 950 μL of isopropanol. The mixture was subjected to ultrasound for a duration of 30 min. Following this, 8 μL of the ink was applied onto a 5 mm diameter (0.5 cm width, 1 cm length) glassy carbon electrode. Measurements were subsequently done in a 1 M KOH solution saturated with O_2. Electrochemical impedance spectroscopy (EIS) measurements were conducted at 0.9 V relative to the reversible hydrogen electrode (RHE). The frequency range used for EIS ranged from 0.01 Hz to 100 000 Hz (or 10^{-2} Hz to 105 Hz in scientific notation), and an amplitude of 10 mV was applied during the measurements. At the same time, the water splitting activity of the catalyst was evaluated using a glassy carbon electrode with a diameter of 5 mm ($\Phi = 5$ mm). To ensure that

the catalyst adhered firmly to the electrode surface during electrochemical testing, the amount of Nafion used was increased to 100 μL. This setup allowed for comprehensive characterization of both the electrochemical impedance and OER/HER performance of the catalyst under controlled experimental conditions.

Furthermore, an electrochemical experiment was conducted using a 1.0 M KOH solution, where all potentials were recorded in relation to the reversible hydrogen electrode (*vs.* RHE). The experiment involved performing linear sweep voltammetry (LSV). The solution used was a 1 M potassium hydroxide (KOH) solution that was saturated with oxygen (O_2). A standard three-electrode setup was utilized with an O_2-saturated 1 M KOH solution to test how well the catalyst performed in both the OER and the HER. All measurements of electrode potentials were referenced against the reversible hydrogen electrode (RHE) using a specific calibration equation (eqn (1)).

$$E_{RHE} = E_{Hg/HgO} + 0.0592pH + 0.098 \text{ V} \tag{1}$$

3.   Results and discussion

3.1.   Preparation and characterization of TiNbC/MOF@SA-H

This work presents the preparation of a new TiNbC/MOF and sodium alginate hydrogel, which is employed for the first time as a supercapacitor to efficiently facilitate the OER and HER.

The experimental setup is shown in Scheme 1. Moreover, morphology significantly influences material performance; hence, it is essential to assess the samples produced by FESEM and EDX tests. The synthesized TiNbAlC MAX phase is shown in Fig. 1a. The TiNbC nanosheets, characterized by increased interlayer spacing, were effectively exfoliated by the etching of the Al layer from the TiNbAlC MAX phase, as shown in Fig. 1b. The clear and lightweight flakes of MXene nanosheets (Fig. 1b) indicate that the bulk MAX phase, as shown in Fig. 1a, has been completely exfoliated into ultrathin 2D nanosheets. Additionally, the *in situ* synthesis of MOF nanomaterials on the TiNbC MXene surface was effectively achieved, as shown in Fig. 1c. There is clear growth of the MOF on the surface of 2D

nanosheets, visible to the naked eye. In addition, with incorporating in sodium alginate polymer hydrogel the small round ball shape as shown in Fig. 1d original image with camera and SEM together with high magnification images (Fig. 1e) of TiNbC/MOF@SA-H composite material with dark contrast uniformly anchored on the sodium alginate polymer hydrogel. Fig. 1f displays the SEM image of the cross-section of the TiNbC/MOF@SA-H hydrogel, characterized by a spherical shape and a rough surface. The surface roughness resulting from the integration of the TiNbC/MOF composite material is shown in Fig. 1f, which confirms the effective incorporation of the MXene and MOF into the hydrogel. Moreover, EDS mapping images of Ti, Nb, Zn, Co and Na for a hydrogel (TiNbC/MOF@SA-H) are
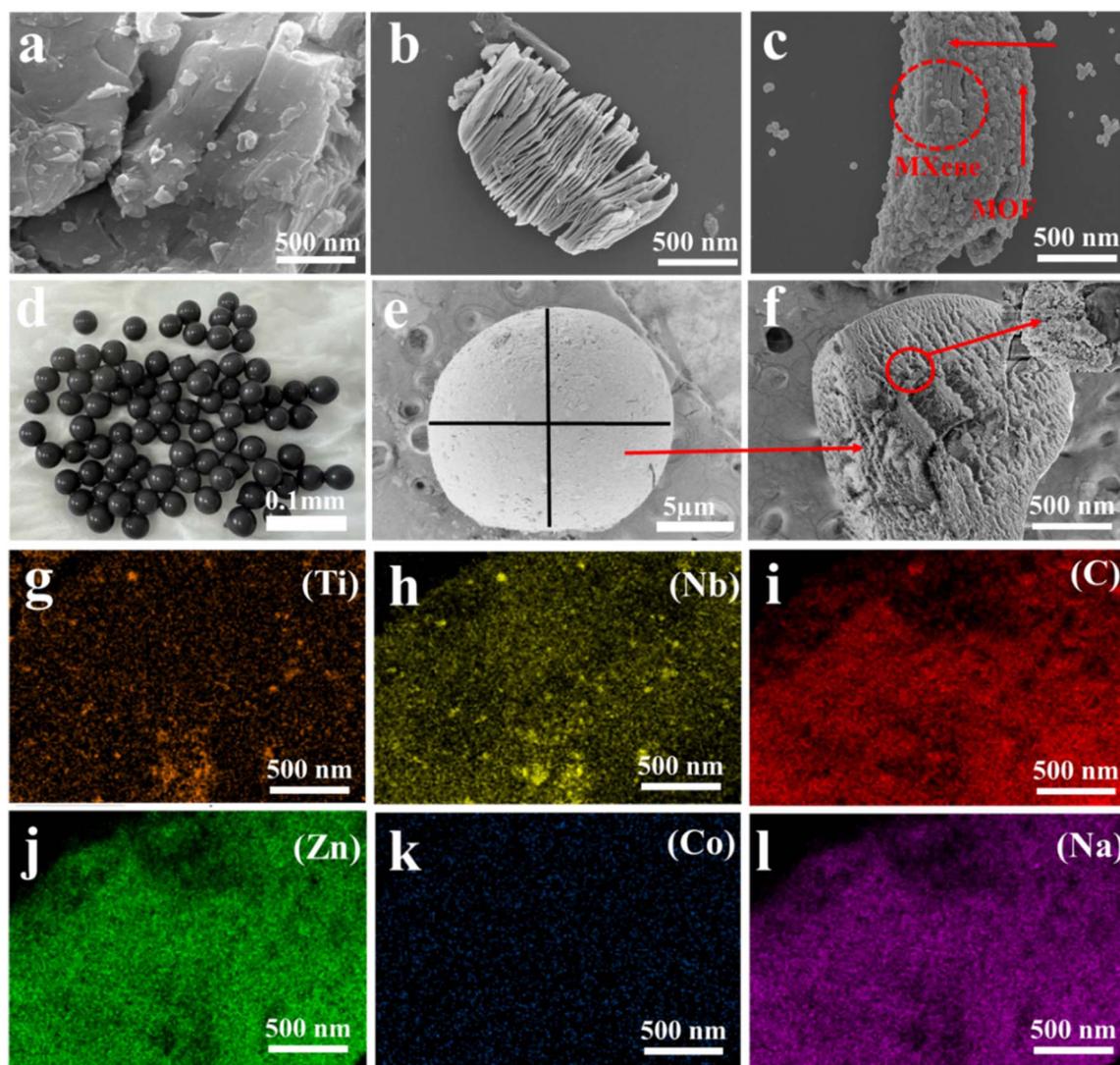

Fig. 1 The SEM images provide a detailed morphological comparison of the materials at various stages. Image (a) of the TiNbAlC MAX phase shows a dense, layered structure typical of MAX phases. After etching to produce TiNbC MXene, image (b) reveals a delaminated, flake-like morphology, indicative of the MXene structure. Image (c) of TiNbC/MOF shows the integration of MOFs, with a more porous structure due to the presence of the metal–organic frameworks. The original picture (d) of the TiNbC/MOF@SA-H hydrogel demonstrates the hydrogel appearance. SEM image (e) of the TiNbC/MOF@SA-H hydrogel shows a highly porous structure, essential for its functional properties. The cross-section (f) reveals internal network structures, suggesting good dispersion of components within the hydrogel matrix. In images (g–l), the EDX mapping of the TiNbC/MOF@SA-H hydrogel highlights the elemental distribution within the composite, confirming the presence of key elements such as Ti, Nb, C, O, Zn, and others from both the MOF and the hydrogel, ensuring uniform integration of all components.

4394 | *J. Mater. Chem. A*, 2025, **13**, 4390–4403

This journal is © The Royal Society of Chemistry 2025

shown in Fig. 1g–l, which confirm the equal distribution of TiNbC/MOF nanosheet elements inside TiNbC/MOF@SA-H. The findings of the SEM morphology and EDX characterization indicate that the preparation of the TiNbC/MOF@SA-H polymer hydrogel was successful and the overall results are satisfactory.

Furthermore, the XRD patterns of the collected pristine Max-phase TiNbAlC, bare TiNbC, TiNbC/MOF nanocomposite, and TiNbC/MOF@SA-H hydrogel materials are compared in Fig. 2A. This figure also shows us the differences between these structures. Utilizing X-ray diffraction patterns, the crystalline structures of pure Max-phase TiNbAlC and bare TiNbC nanosheets were analyzed and assessed. After etching, the pure Max-phase TiNbAlC and bare TiNbC samples, as shown in Fig. 2A(a and b), display the characteristic 002 reflections at $2\theta = 6.9°$. These reflections correspond to the pristine Max phase and typical exfoliated nanosheets of MXene. A further point to consider is that the crystalline structure of pure Max-phase TiNbAlC and bare TiNbC exhibits distinct diffraction peaks, as shown in Fig. 2A(a and b). The XRD pattern of the TiNbC/MOF nanocomposite reveals that this reflection shifts to the nanocomposite and polymer hydrogel 2θ position of 6.9° with a reduced peak intensity, suggesting that TiNbC MXene is successfully incorporated into the polymer hydrogel. Following

the *in situ* development of the MOF on the surface of TiNbC, XRD reveals all of the structural crystals on the MXene peak from 6.9° to 9.9° and from 21.8o to 74.3o, indicating that the growth of the MOF on the surface of (TiNbC) MXene was successful.[56] Moreover, after the synthesis of polymer hydrogel materials, all the diffraction peaks were seen in the TiNbC/MOF@SA-H hydrogel, which served as evidence that the hydrogel materials were successfully prepared.

The FT-IR spectra of the four materials, pristine Max-phase TiNbAlC$_2$, bare TiNbC, TiNbC/MOF nanocomposite, and TiNbC/MOF@SA-H hydrogel, are shown in Fig. 2B. The pure Max-phase TiNbAlC$_2$ and bare TiNbC exhibited no discernible peaks, possibly due to some errors. However, for the TiNbC/MOF nanocomposite and TiNbC/MOF@SA-H hydrogel materials, as shown in Fig. 2B(c and d), the observed peaks at 1605 cm^{-1} correspond to the stretching vibrations of the C–O single bond. The absorption peaks observed near 1425 cm^{-1} and 1075 cm^{-1} signify the characteristic stretching vibration of the C–O–C bond. Furthermore, the TiNbC/MOF@SA-H polymer hydrogel displayed pronounced peaks between 3500 and 3000 cm^{-1}, presumably attributable to the existence of C–H bonds and carboxylic bonds inside the hydrogel. This spectral range corresponds to vibrations associated with these chemical groups, indicating their presence in the material. These bonds
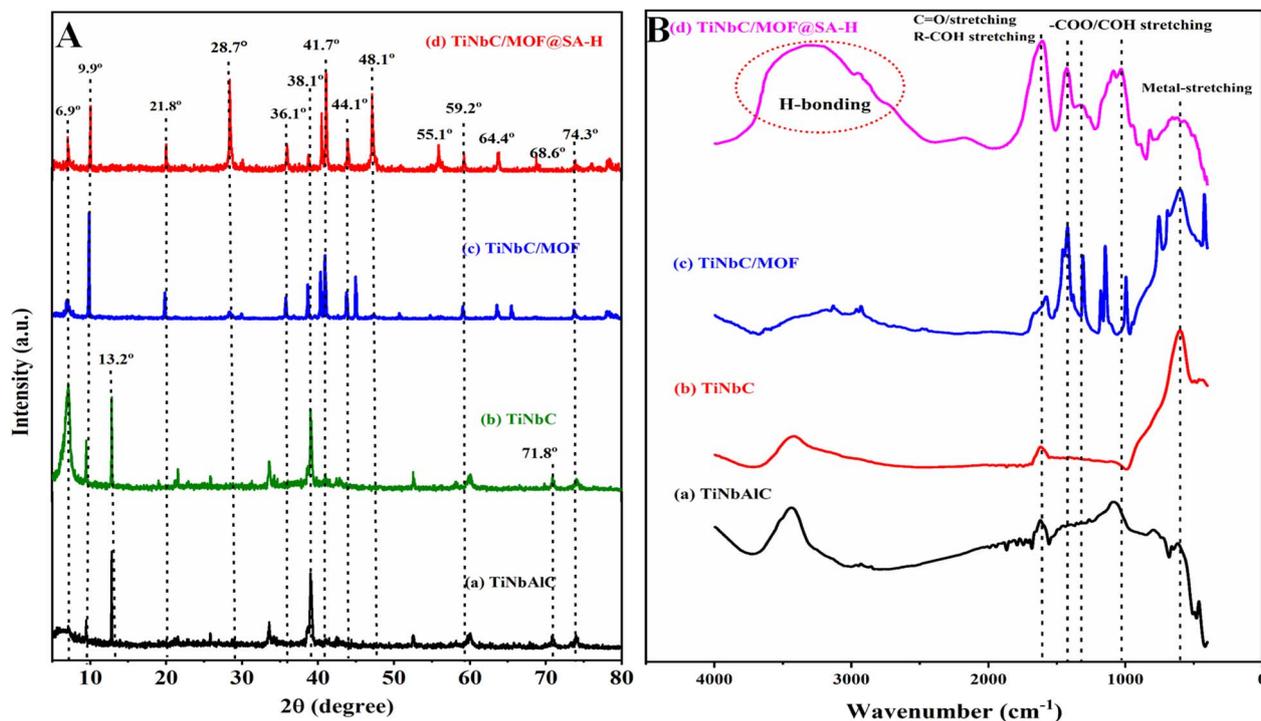

Fig. 2 In the XRD spectra (A), different materials are compared to identify their crystalline structures. The spectrum of TiNbAlC (a) displays the characteristic peaks of the MAX phase structure, indicating its well-ordered layered nature. Upon selective etching of aluminum, TiNbC (b) shows a shift and sharpening of peaks corresponding to a transition into an MXene structure. In TiNbC/MOF (c), additional peaks emerge, signifying successful integration of MOFs into the MXene. TiNbC/MOF@SA-H (d) reveals further peak modifications, suggesting the inclusion of a sodium alginate hydrogel, indicating a structural change due to hybridization. For the FTIR spectra (B), the TiNbC (b) spectrum exhibits characteristic bands associated with Ti–C and Nb–C vibrations. In TiNbC/MOF (c), new bands emerge corresponding to organic linkers in the MOF, confirming its presence. The TiNbC/MOF@SA-H (d) spectrum shows additional peaks related to the sodium alginate hydrogel, indicating functional groups such as O–H and C–O, suggesting successful composite formation.

This journal is © The Royal Society of Chemistry 2025

J. Mater. Chem. A, 2025, **13**, 4390–4403 | **4395**

are crucial as they contribute to the structural integrity and functional properties of the hydrogel, potentially influencing its performance in various applications such as catalysis or energy storage. Overall, these data are enough for the formulation of a polymer hydrogel.

Furthermore, AFM analysis was performed for the surface roughness of Max-phase, MXene, TiNbC/MOF, and TiNbC/MOF@SA-H hydrogel, as shown in Fig. 3. The first measurements focused on investigating the feasibility of imaging these hydrogels, as well as the impact of MXene preparation and MOF development on the surface and the inclusion of alginate on the surface morphology. Fig. 3a–d displays AFM height images and their corresponding 3D representations of Max-phase, MXene, TiNbC/MOF, and TiNbC/MOF@SA-H hydrogel. The sequential deposition of the MOF onto the MXene surface, followed by its integration into the alginate hydrogel, resulted in a decrease in surface roughness. This is evident from the example surface profiles shown in Fig. 3a–d, as well as the lowered estimated mean roughness value of $R_a = 1.05$ nm for Max-phase, $R_a = 6.73$ nm for TiNbC, $R_a = 7.99$ nm for TiNbC/MOF and $R_a = 12.3$ nm for the TiNbC/MOF@SA-H hydrogel, respectively. By examining the color scales in the various images, it is evident that there is a consistent pattern. The relative height range increases as the MOF grows on the surface of MXene and is subsequently incorporated into the alginate hydrogel (Fig. 3a–d). In addition, Fig. 3e–h support the statements of surface roughness after growth and incorporation into the alginate hydrogel. Additionally, the TGA analysis, shown in Fig. S1,† offers significant insights into the thermal stability and breakdown characteristics of the examined materials. The disparities in weight loss patterns between the TiNbC/MOF nanocomposite and TiNbC/MOF@SA-H samples highlight the significance of comprehending the structural and compositional alterations caused by surface modification and their impact on thermal performance.

Furthermore, Fig. 4a displays the XPS survey spectrum of all the elements (Nb, Zn, C, Ti, O, Na, and Ca) in TiNbC/MOF@SA-H hydrogel materials, illustrating the presence of all elements and confirming the electrostatic connection between TiNbC, MOF nanosheets, and the polymer hydrogel. Additionally, the C 1s XPS spectrum shown in Fig. 4b reveals surface oxidation, as indicated by the C=C, C–O–C, and O–C=O peaks at 284.5, 286.3, and 288.3 eV, respectively. Besides, Fig. 4c illustrates the O 1s spectrum exhibiting two peaks corresponding to C–O and C=O stretching vibrations at 531.3 eV and 532.4 eV, respectively. In addition, Fig. 4d presents the Nb 3d spectrum of the MXene, revealing two prominent peaks, Nb $3d_{3/2}$ and Nb $3d_{5/2}$, at 198.2 eV and 200.1 eV, respectively. Moreover, Fig. 4e shows two peaks in the Ti 2p spectrum, with the Ti $2p_{3/2}$ XPS peak at 458.4 eV exhibiting lower intensity, indicating a greater oxidation state of Ti^{4+}. The Ti $2p_{1/2}$ displays a smaller peak at 464.1 eV.[57]

In addition, Zn 2p from the MOF shows two high intensity peaks corresponding to Zn $2p_{3/2}$ and Zn $2p_{1/2}$ at peak intensities of 1022.1 and 1044.8 eV. The Ca 2p from the polymer hydrogel Ca $2p_{3/2}$ and Ca $2p_{1/2}$ provide the two peaks at highest intensity of 347.6 and 351.1 eV, confirming the existence of Ca elements in the polymer hydrogel (Fig. 4g). Furthermore, the Na 1s element from the polymer hydrogel shows a high intensity Na–O peak at a binding energy of 1072.0 eV, as shown in Fig. 4h. The MXene elements Ti–C, Nb, and elements from MOF Zn and Co bonding from the TiNbC/MOF component in the high-resolution. The *in situ* synthesis of the MOF on the surface of TiNbC MXene by a self-assembly technique facilitates efficient electrochemical bonding. These findings validate the existence of Ti, Zn, Co, and Na in a mixed valence state, which is advantageous for HER and OER applications. The shift of the peak towards higher wavenumbers and increased intensity signified the emergence of new materials. The discovery indicates that the existence of this peak
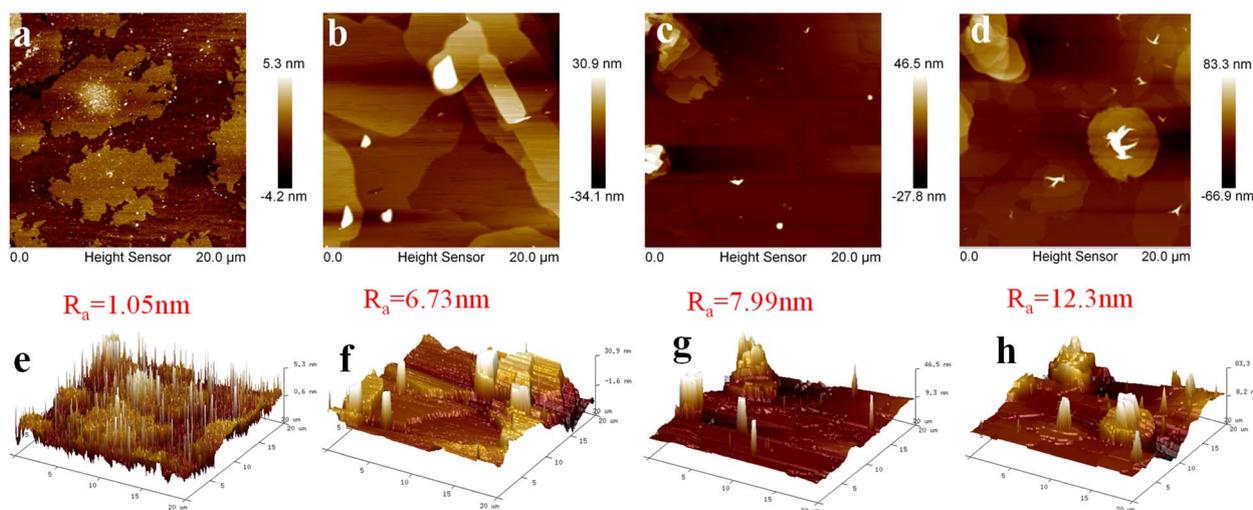

Fig. 3 AFM is used to capture height images and create 3D representations of surfaces. Additionally, AFM can measure the relative height roughness of a surface: (a) TiNbAlC, (b) TiNbC, (c) TiNbC/MOF and (d) TiNbC/MOF@SA-H. Furthermore, the images (e–h) represent the surface profile of a random horizontal line and roughness.
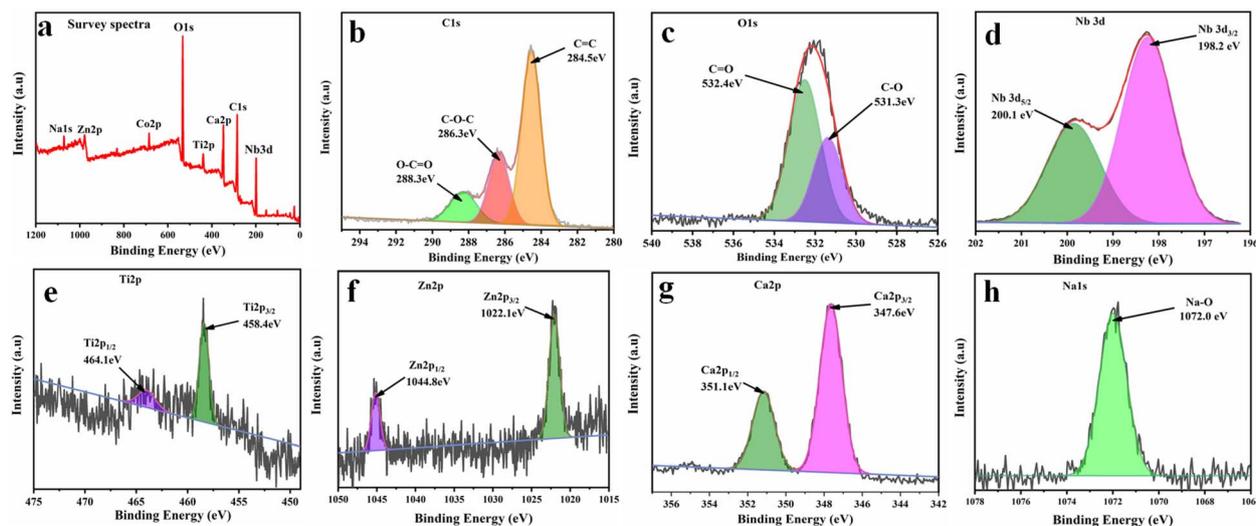
4396 | *J. Mater. Chem. A*, 2025, **13**, 4390–4403

This journal is © The Royal Society of Chemistry 2025

Fig. 4 The XPS analysis of the TiNbC/MOF@SA-H composite provides insight into the chemical states and elemental composition. The XPS survey spectrum (a) confirms the presence of elements like C, O, Nb, Ti, Zn, Ca, and Na in the sample. The C 1s spectrum (b) shows peaks corresponding to C=C, C−O, and C=O bonds, indicating the presence of carbon-related functional groups. The O 1s spectrum (c) reveals peaks for C−O−Ti and O−C bonds, confirming oxide formation. (d) Nb 3d and Ti 2p (e) spectra show their respective oxidation states, verifying their incorporation in the composite. Zn 2p (f) and Ca 2p (g) peaks indicate contributions from MOF components, while Na 1s (h) corresponds to sodium ions in the SA-H matrix, confirming their interaction within the structure.

is attributable not just to surface groups but also to the interactions among individual flakes.

3.2. Hydrogen evolution reaction

The hydrogen evolution reaction (HER) catalytic activity of several produced catalysts (TiNbC/MOF and TiNbC/MOF@SA-H

polymer hydrogel) was evaluated in alkaline electrolytes (1 M KOH), alongside the noble metal catalyst (Pt/C, 20 wt%), as shown in Fig. 5. Based on experimental findings, the remarkable progress in TiNbC/MOF electron transfer may be used as an efficient approach to modify the synthesized TiNbC/MOF@SA-H for the hydrogen evolution reaction. An electrochemical setup was used to investigate the properties of
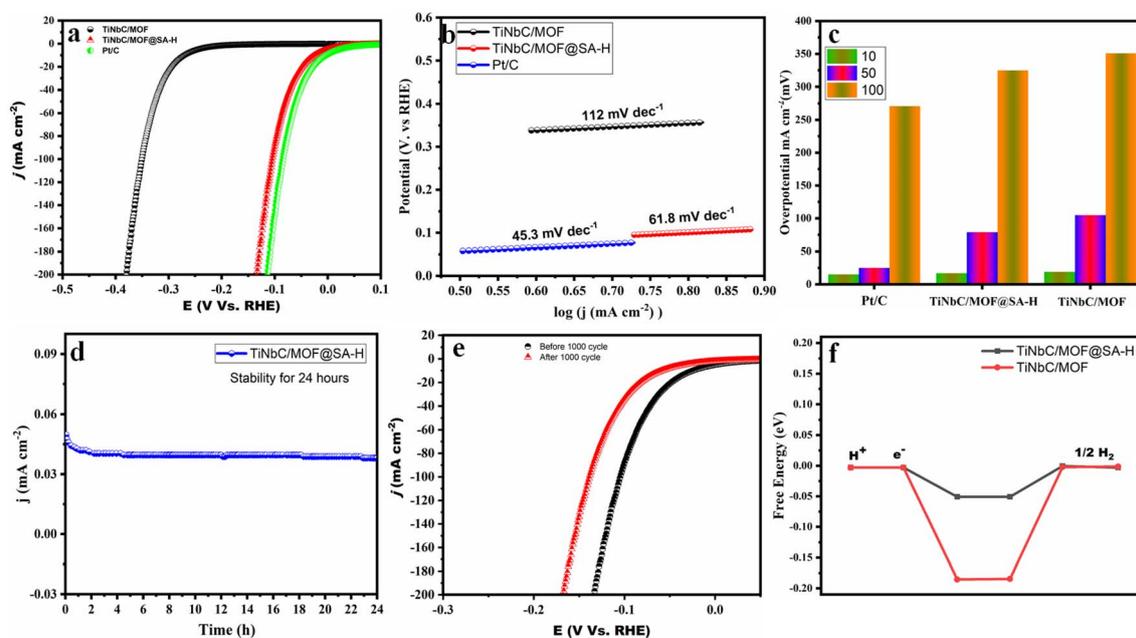

Fig. 5 (a) HER polarization LSV curves, (b) HER Tafel slope, (c) overpotential of all the samples with $\eta = 10$, 50 and 100 mA cm^{-2} (mV) for Pt/C, TiNbC/MOF and TiNbC/MOF@SA-H, (d) stability curve for 24 h, (e) LSV curve before and after 1000 CV cycles, and (f) free energy curve (eV) of TiNbC/MOF and TiNbC/MOF@SA-H.

electrocatalysis. The catalytic performance of TiNbC/MOF and TiNbC/MOF@SA-H electrocatalysts for the HER was evaluated using LSV. Fig. 5a illustrates the polarization curves of Pt/C, TiNbC/MOF, and TiNbC/MOF@SA-H samples obtained at a scan rate of 5 mV s^{-1}.

The Tafel slope was used to more accurately assess the kinetics of the HER (Fig. 5b). Compared to Pt/C, our materials TiNbC/MOF and TiNbC/MOF@SA-H have much faster kinetics, with Tafel slope values of 112 and 61.6 mV dec^{-1}, respectively. These values are consistent with their high catalytic activity. Nevertheless, the literature often cites values between 30 and 60 mV dec^{-1} for the HER when discussing Pt/C catalysts.[58,59] Fig. 5c illustrates that TiNbC/MOF@SA-H exhibits superior HER catalytic activity compared to the other synthesized samples, necessitating just 17, 79, and 325 mV to achieve current densities of 10, 50, and 100 mA cm^{-2}, respectively. TiNbC/MOF@SA-H demonstrates catalytic performance for the hydrogen evolution reaction (HER) that is comparable to that of the benchmark catalyst Pt/C. The comparison study of MOF@SA-H and TiNbC@SA-H is also included in the ESI Fig. S3,† which shows a lower HER catalytic ability as compared with the final TiNbC/MOF@SA-H materials.

This overpotential is lower than that of TiNbC/MOF and TiNbC/MOF@SA-H, indicating their effective performance in the HER and exhibiting very close HER catalytic performance compared to 20% Pt/C, as depicted in Fig. 5c. This indicates that TiNbC/MOF@SA-H is more effective at generating hydrogen gas under the above-mentioned conditions, highlighting its potential as an efficient catalyst for HER applications. The diminished HER activity observed in TiNbC/MOF without the introduction of hydrogel species is primarily due to the restricted exposure of active sites caused by material aggregation. This underscores the critical role played by dispersed single atoms such as Ti, Zn, and Co as active centers in facilitating the HER catalytic process. The TiNbC/MOF@SA-H electrocatalysts demonstrated remarkable durability in the accelerated stability test after 1000 CV cycles and LSV scans (Fig. 5d), showing only a slight reduction in the cathodic current from the initial to the 1000th cycle.[60] Additionally, the long-term stability test, conducted for over 24 h in an alkaline medium (1 M KOH) at an overpotential of 10 mV, further confirmed their robustness. This stability underscores their potential for practical applications in the hydrogen evolution reaction. The study found that the TiNbC/MOF@SA-H composite material exhibited sufficient stability during the HER. This indicates that integrating titanium niobium carbide (TiNbC) with metal–organic frameworks (MOFs) on a substrate (SA-H) enhances the material's durability under reaction conditions. Such stability is essential for real-world applications in water splitting and renewable energy systems, as it ensures that the catalyst remains effective and intact over prolonged use.

This satisfactory HER stability highlights the material's potential for efficient and sustainable hydrogen production. Moreover, the more favorable HER activity of the designed TiNbC/MOF@SA-H polymer hydrogel would inspire new directions in designing MXene, MOF and polymer hydrogel based electrocatalysts with excellent performance for alkaline HER

and beyond. Fig. 5e shows the LSV after and before the 1000 CV cycles, which provide satisfactory results.[61] In short, the TiNbC/MOF@SA-H polymer hydrogel demonstrates exceptional performance in electrocatalytic hydrogen evolution, characterized by low overpotentials, rapid kinetics, and significant durability. Furthermore, the electronic structures of TiNbC/MOF and TiNbC/MOF@SA-H were analyzed to understand the physical mechanism behind their weak adsorption of intermediates during the HER, as described in Fig. 5f. TiNbC/MOF@SA-H exhibited superior activity with nearly optimized levels (almost zero), indicating minimal adsorption of HER intermediates, which is crucial for enhancing catalytic performance. These findings underscore its potential as a highly efficient and stable catalyst for sustainable hydrogen production in applications such as water splitting and renewable energy technologies. The study's findings suggest that coating TiNbC with MOFs on an SA-H substrate is a promising strategy for developing advanced electrocatalysts.

The HER cyclic voltammetry (CV) profiles of double-layer capacitance (C_{dl}) serve as an indicator for estimating the electrochemically active surface area (ECSA) of the two catalysts and one reference (Pt/C), determined at varying scan rates from 5 to 100 mV s^{-1} in the non-faradic reaction region, as shown in Fig. 6a. The ECSA is a crucial parameter for assessing the real active area, which may be evaluated by analyzing CV curves at various scan speeds in the non-faradaic region and observing the slope of the fitted line. The C_{dl} of the TiNbC/MOF@SA-H electrocatalyst (22.4 mF cm^{-2}) is close to that of the reference (33.7 mF cm^{-2}) and higher than that of TiNbC/MOF (12.2 mF cm^{-2}), indicating that TiNbC/MOF@SA-H has the largest electrocatalytically active surface area (Fig. 6b). These properties reveal the excellent HER activity of TiNbC/MOF@SA-H. Moreover, at lower scan rates, distinct pairs of redox peaks were visible, which broadened at higher scan rates.[62] This behavior suggests that the TiNbC/MOF@SA-H electrode employs an intercalated pseudocapacitive energy storage mechanism when used in a basic electrolyte. Therefore, the TiNbC/MOF@SA-H hydrogel electrode demonstrates a remarkable ability to maintain a high gravimetric capacitance along with exceptional rate capability. This performance highlights the essential contribution of the synergistic relationship between the electrode's vertically aligned macrostructure and its proton-intercalated microstructure. This interaction enhances the efficiency of charge and ion transport, leading to improved overall performance.

3.3. Oxygen evolution reaction

The self-assembled *in situ* TiNbC/MOF and TiNbC/MOF@SA-H hydrogel provide exceptional electrochemical water oxidation performance as working electrodes. These electrodes may be employed immediately without the need for drying or any other substances. Furthermore, they exhibit great wettability for basic electrolytes (1 M KOH). The TiNbC/MOF and TiNbC/MOF@SA-H hydrogel were examined in a 1 M O$_2$-saturated KOH solution using a three-electrode setup. For comparative purposes, commercial IrO$_2$ was also evaluated under the same settings.
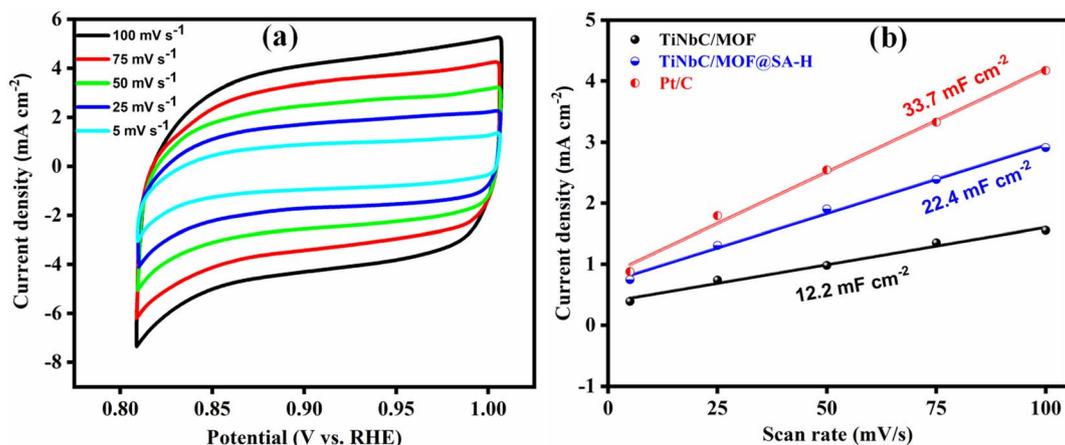
4398 | *J. Mater. Chem. A*, 2025, **13**, 4390–4403

This journal is © The Royal Society of Chemistry 2025

Fig. 6 (a) HER CV curve of TiNbC/MOF@SA-H at various scan rates (5–100 mV s^{-1}) and (b) C_{dl} capacitance of Pt/C, TiNbC/MOF and TiNbC/MOF@SA-H.

The catalytic efficiency of TiNbC/MOF and TiNbC/MOF@SA-H hydrogel electrocatalysts in the OER was assessed using LSV.[63] This technique involves sweeping the electrode potential linearly over a range while measuring the resulting current. By analyzing the voltammograms obtained, researchers can determine the catalysts' performance in terms of their ability to facilitate these electrochemical reactions. The onset potential for the OER of the TiNbC/MOF@SA-H hydrogel (100 ms-P) was determined to be 1.4 V. This value is lower than the onset potential of both TiNbC/MOF and IrO$_2$. The results illustrated in Fig. 7a clearly indicate that the sample treated with a rapid and pulsed method shows the highest level of catalytic activity. Specifically, the TiNbC/MOF@SA-H hydrogel exhibits a significantly lower onset potential of 1.4 V (*versus* the reversible

hydrogen electrode) at a current density of 1 mA cm^{-2} compared to the other catalysts used in the study. This lower onset potential promotes the formation of the reaction intermediate TiNbC/MOF@SA-H hydrogel. The electrochemical performance the OER polarization curve of pristine IrO$_2$, MXene/MOF composite and MXene/MOF@SA-H hydrogel were evaluated in a three-electrode configuration (Fig. 7a).[64] The MXene/MOF composite and MXene/MOF@SA-H hydrogel have very low overpotentials for the oxygen evolution reactions (OER), as shown in Fig. 7b. Specifically, at 10 mV overpotentials are measured to be 66, 84, and 145 mA cm^{-2}, respectively. These values surpass those of the catalysts commonly reported in the literature. In addition, Fig. 7b illustrates the analysis of Tafel plots to assess the kinetics of the electrodes. The MXene/
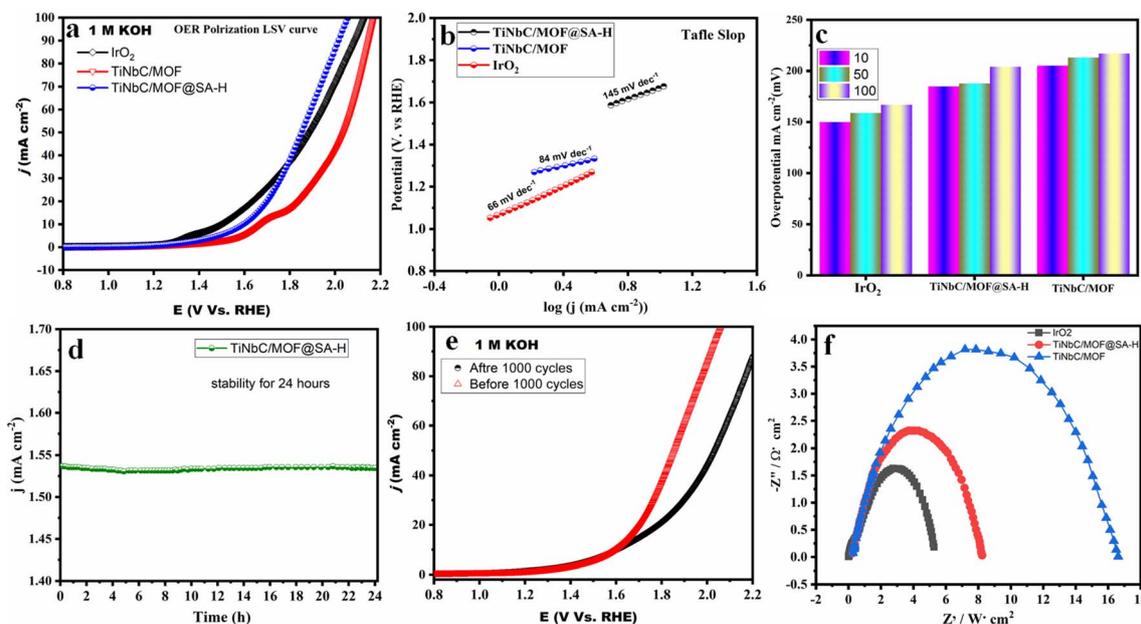

Fig. 7 (a) OER polarization LSV curves, (b) Tafel slope, (c) the overpotentials required for achieving η = 10, 50 and 100 mA cm^{-2} (mV), (d) stability curve for 24 h, (e) KOH LSV curve after and before 1000 cycles, and (f) Nyquist plots at 4.0 V$_{RHE}$ of IrO$_2$, TiNbC/MOF and TiNbC/MOF@SA-H.

MOF@SA-H hydrogel has a Tafel slope of just 84 mV dec^{-1}, indicating much quicker kinetics for the OER.

Furthermore, TiNbC/MOF@SA-H exhibits superior OER electrocatalytic activity compared to the reference IrO$_2$ and the composite TiNbC/MOF, by exhibiting a low overpotential of 185, 188 and 204 mV at 10, 20, and 50 mA cm^{-2}, respectively, as illustrated in Fig. 7c. These overpotentials are only slightly larger than those of IrO$_2$ (150, 159 and 167 mV at 10, 50 and 100 mA cm^{-2}). However, the TiNbC/MOF showed a lower overpotential (see Fig. 7c), which is primarily due to the limited exposure of active sites caused by material aggregation. In addition, the OER comparison study of MOF@SA-H and TiNbC@SA-H catalysts was also included in the ESI, Fig. S4,† which shows a very low OER catalytic ability as compared to the final material (TiNbC/MOF@SA-H). This highlights the critical role of dispersed single atoms such as Ti, Zn, Co, Na, and Ca as active centers in the OER catalytic process. Additionally, electrochemical stability is essential for large-scale applications; without it, widespread use is not feasible. Therefore, long-term stability serves as a crucial metric for evaluating electrocatalysts. The stability of the MXene/MOF@SA-H polymer hydrogel over 24 h was also assessed, as depicted in Fig. 7d. The results indicate that the composite material TiNbC/MOF@SA-H demonstrated outstanding stability in alkaline media. This stability suggests that the combination of TiNbC with MOFs, supported by SA-H, creates a synergistic effect that enhances the durability of the catalyst under operational conditions. Remarkable stability is crucial for practical applications in water splitting and renewable energy technologies, where consistent and long-term performance is required. The excellent OER stability implies that the material maintains its catalytic efficiency and structural integrity over extended periods, making it a promising candidate for efficient and sustainable oxygen production.

Further, Fig. 7e shows LSV polarization curves before and after 1000 CV cycles, which show satisfactory polarization ability and confirmation. Besides, the value of charge transfer resistance (R_{ct}) was also calculated as shown in Fig. 7f, for TiNbC/ MOF@SA-H ($\sim$2.025 Ω), as compared to reference IrO$_2$ become is ($\sim$1.75 Ω) almost near to (R_{ct}) the value of TiNbC/ MOF@SA-H, while the TiNbC/MOF ($\sim$3.56 Ω) and this improved electronic structure of the catalysts is primarily attributed to the entry of Ti, Zn, Co, Na, and Ca atoms from the hydrogel. This modification leads to an increase in charge transfer capacity and conductivity during the HER. In conclusion, the TiNbC/MOF@SA-H hydrogel demonstrates exceptional electrochemical water oxidation performance, characterized by low onset potentials, ultralow overpotentials, rapid OER kinetics, and excellent stability. These characteristics highlight its potential as an efficient and durable electrocatalyst for sustainable oxygen production through water splitting and renewable energy technologies.

The OER cyclic voltammetry (CV) profiles were obtained at scan rates from 5 to 100 mV s^{-1}, as shown in Fig. 8a. At lower scan rates, distinct pairs of oxidation peaks were visible, which broadened at lower scan rates. This behavior suggests that the TiNbC/MOF@SA-H electrode employs an intercalated pseudo-capacitive energy storage mechanism when used in a basic electrolyte. Interestingly, the largest C_{dl} occurring in TiNbC/ MOF@SA-H is 9.43 mF cm^{-2} (Fig. 8b), illustrating the high specific surface area and numerous active sites coupled with the structural characteristics of the catalyst. This performance underscores the critical role of the synergistic interaction between its vertically aligned macrostructure and proton-intercalated microstructure, which facilitates faster charge and ion transport.

3.4. Possible mechanistic pathway

The simple mechanism pathways for both oxygen and hydrogen evolution are represented in Fig. 9. In this illustration, the active sites within the polymer hydrogel's 3D framework are formed by incorporating Ti, Zn, Co, and Na atoms. The pathways for the 4-electron (4e$^-$) and 2-electron (2e$^-$) mechanisms of the OER and HER are outlined, including the optimized structures of the intermediates in the two-step process for TiNbC/MOF@SA-H. These detailed illustrations provide a clear understanding of
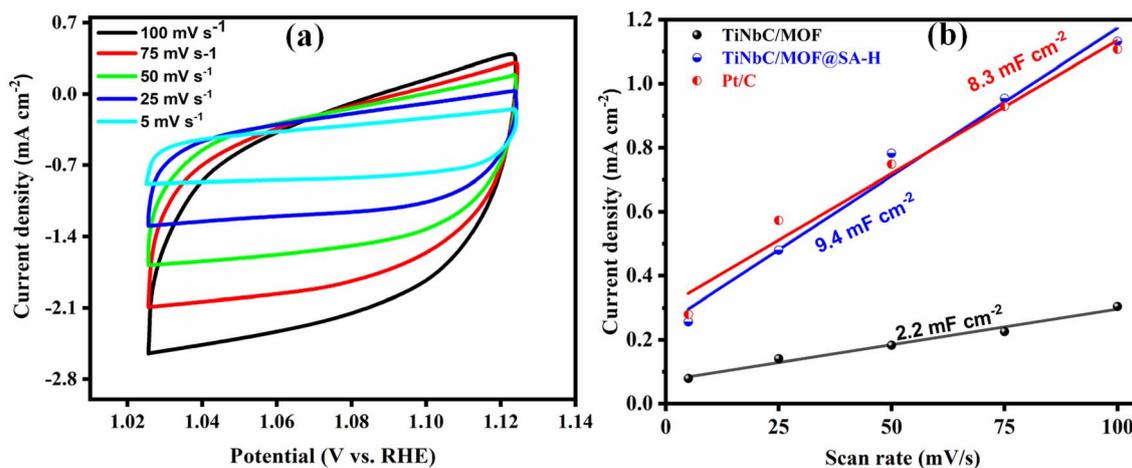

Fig. 8 (a) OER CV curve of TiNbC/MOF@SA-H at various scan rates (5–100 mV s^{-1}) and (b) C_{dl} capacitance of Pt/C, TiNbC/MOF and TiNbC/ MOF@SA-H.

4400 | J. Mater. Chem. A, 2025, 13, 4390–4403
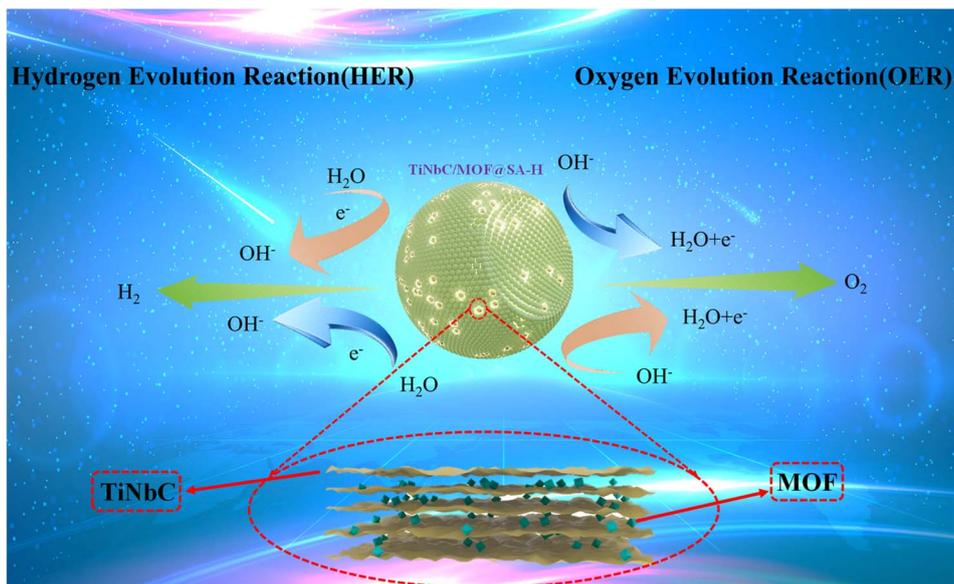
This journal is © The Royal Society of Chemistry 2025

Fig. 9 The proposed mechanism for TiNbC/MOF@SA-H as an electrocatalyst in the HER and OER involves synergistic effects between the MXene (TiNbC), MOF, and sodium alginate hydrogel (SA-H). In the HER, TiNbC provides active sites with excellent electrical conductivity, facilitating electron transfer, while the MOF enhances proton adsorption and promotes hydrogen evolution due to its high surface area and porosity. The SA-H hydrogel offers a hydrated environment, improving ion transport.

the catalytic activities and structural configurations involved in the reactions. The *in situ* incorporation of single atoms of Ti, Zn, and Co within the polymer hydrogel's 3D framework significantly boosts the generation of free electrons during charge–discharge cycles on the electrodes. This abundant supply of free electrons enhances the adsorption capabilities of hydroxide ions (OH^-) and hydrogen ions (H^+), facilitating more effective catalytic processes.[65] The improved adsorption is evident from the differences in the charge density distribution shown in Fig. 9. This strategic placement of atoms not only optimizes the active sites for the reactions but also enhances the overall efficiency and performance of the electrode material in electrochemical applications. Incorporating multiple metal atoms, such as Ti, Zn, and Co, into the lattice of the hydrogel structure significantly alters the electronic configuration. This redistribution of the electronic structure creates a more favorable electronic environment, improving the effectiveness of the catalytic processes involved in both the HER and the OER to increase efficiency. The optimized electronic environment facilitates better interaction with reactants, leading to improved catalytic performance.

4. Conclusion

In summary, this study successfully introduces a novel multifunctional material, MXene@MOF integrated with a SA hydrogel (TiNbC/MOF@SA-H), demonstrating its potential as a high-performance electrocatalyst for energy storage and conversion applications. By etching the TiNbAlC Max-phase to produce MXene (TiNbCTx), followed by its combination with a MOF through a meticulous process involving methanol dispersion, ultrasonication, and subsequent integration with zinc and cobalt nitrate, the research team achieved the synthesis of

TiNbC@MOF. Incorporating this compound into a SA hydrogel further enhanced its functional properties. Comprehensive structural characterization using SEM, EDX, XRD, FTIR, AFM, TGA, and XPS confirmed the successful synthesis and integration of components. Electrocatalytic performance evaluations revealed exceptional results, with TiNbC/MOF@SA-H exhibiting a Tafel slope of 84 mV dec^{-1} for the OER and 61.8 mV dec^{-1} for the HER at a 1 V s^{-1} scan rate. TiNbC/MOF@SA-H demonstrates exceptional OER electrocatalytic performance compared to the reference IrO_2 and composite TiNbC/MOF. It achieves low overpotentials of 185, 188, and 204 mV at current densities of 10, 20, and 50 mA cm^{-2}, respectively. Additionally, it shows superior HER catalytic activity compared to the other synthesized samples, requiring only 17, 79, and 325 mV to reach current densities of 10, 50, and 100 mA cm^{-2}, respectively. Notably, the material demonstrated remarkable stability, maintaining performance over 1000 cycles for 24 h without mass loss. The innovative approach detailed in this study provides a straightforward and effective method for constructing high-performance hydrogel electrodes, marking a significant advancement in the development of clean energy technologies.

Data availability

Data is available free of charge on the website of the Royal Society of Chemistry.

Author contributions

Saleem Raza and Ata Ur Rehman: conceptualization, investigation, writing – original draft, and writing – review & editing. Cheng Chen and Tianyu Zhao: writing – review & editing. Asif

Hayat and Tariq Bashir: conceptualization and investigation. Liguo Shen: conceptualization, resources, funding acquisition, and supervision. Yasin Orooji and Hongjun Lin: conceptualization, resources, funding acquisition, and supervision.

Conflicts of interest

The authors declare that they have no competing financial interests.

Acknowledgements

References

1 Y. Shang, S. Sang, A. K. Tiwari, S. Khan and X. Zhao, *Appl. Energy*, 2024, **362**, 122994.

2 C. Fletcher, W. J. Ripple, T. Newsome, P. Barnard, K. Beamer, A. Behl, J. Bowen, M. Cooney, E. Crist, C. Field, K. Hiser, D. M. Karl, D. A. King, M. E. Mann, D. P. McGregor, C. Mora, N. Oreskes and M. Wilson, *PNAS Nexus*, 2024, **3**, 106.

3 Y. Li, Y. Ding, S. He, F. Hu, J. Duan, G. Wen, H. Geng, Z. Wu, H. B. Gooi and Y. Zhao, *Nat. Rev. Electr. Eng.*, 2024, 1–17.

4 J. Tan, X. Wang, W. Chu, S. Fang, C. Zheng, M. Xue, X. Wang, T. Hu and W. Guo, *Adv. Mater.*, 2024, **36**, 2211165.

5 S. Raza, A. Hayat, T. Bashir, C. Chen, L. Shen, Y. Orooji and H. Lin, *Sustainable Mater. Technol.*, 2024, **40**, e00963.

6 M. Reveles-Miranda, V. Ramirez-Rivera and D. Pacheco-Catalán, *Renewable Sustainable Energy Rev.*, 2024, **192**, 114196.

7 J. Zhao, N. Liao and J. Luo, *J. Mater. Chem. A*, 2023, **11**(17), 9682–9690.

8 R. Deng, M. Gao, B. Zhang and Q. Zhang, *Adv. Energy Mater.*, 2024, **14**, 2303707.

9 Y. Li and R. Ding, *Nano Energy*, 2024, **124**, 109430.

10 S. Deebansok, J. Deng, E. Le Calvez, Y. Zhu, O. Crosnier, T. Brousse and O. Fontaine, *Nat. Commun.*, 2024, **15**, 1133.

11 Y. J. Lei, L. Zhao, W. H. Lai, Z. Huang, B. Sun, P. Jaumaux, K. Sun, Y. X. Wang and G. Wang, *Chem. Soc. Rev.*, 2024, **53**, 3829–3895.

12 J. Bai, H. Li, P. Vivegananthan, X. Tian, Y. Dong, J. Sun, Z. Dai and K. Zhou, *Adv. Energy Mater.*, 2024, **14**, 2303035.

13 Z. X. Ge, Y. Ding, T. J. Wang, F. Shi, P. J. Jin, P. Chen, B. He, S. B. Yin and Y. Chen, *J. Energy Chem.*, 2023, **77**, 209–216.

14 W. Bai, L. Shi, Z. Li, D. Liu, Y. Liang, B. Han, J. Qi and Y. Li, *Mater. Today Energy*, 2024, **41**, 101547.

15 Y. Zhou, L. Yin, S. Xiang, S. Yu, H. M. Johnson, S. Wang, J. Yin, J. Zhao, Y. Luo and P. K. Chu, *Adv. Sci.*, 2024, **11**, 2304874.

16 P. Zhang, X. Wang, Y. Zhang, Y. Wei, N. Shen, S. Chen and B. Xu, *Adv. Funct. Mater.*, 2024, 2402307.

17 D. Meng, M. Xu, S. Li, M. Ganesan, X. Ruan, S. K. Ravi and X. Cui, *Small*, 2024, **20**, 2304483.

18 M. Sai Bhargava Reddy and S. Aich, *Coord. Chem. Rev.*, 2024, **500**, 215542.

19 T. J. Wang, L. B. Sun, X. Ai, P. Chen, Y. Chen and X. Wang, *Adv. Mater.*, 2024, 2403664.

20 A. Hanan, M. N. Lakhan, F. Bibi, A. Khan, I. A. Soomro, A. Hussain and U. Aftab, *Chem. Eng. J.*, 2024, **482**, 148776.

21 Q. Xue, Z. Wang, Y. Ding, F. Li and Y. Chen, *Chin. J. Catal.*, 2023, **45**, 6–16.

22 Y. He, H. Sun, Y. Wang, Y. N. Yu, C. Mu and L. Chen, *Chem. Eng. J.*, 2024, **485**, 150047.

23 J. Yang, X. Zeng, M. Tebyetekerwa, Z. Wang, C. Bie, X. Sun, I. Marriam and X. Zhang, *Adv. Energy Mater.*, 2024, **14**, 2400740.

24 X. L. Liu, Y. C. Jiang, J. T. Huang, W. Zhong, B. He, P. J. Jin and Y. Chen, *Carbon Energy*, 2023, **5**(12), e367.

25 L. Lu, G. Guan, J. Wang, W. Meng, S. Li, Y. Zhang and F. Guo, *Chem. Eng. J.*, 2024, **480**, 147999.

26 B. Ouyang, D. Wei, B. Wu, L. Yan, H. Gang, Y. Cao, P. Chen, T. Zhang and H. Wang, *Small*, 2024, **20**, 2303153.

27 Y. Xie, X. Wu, Y. Shi, Y. Peng, H. Zhou, X. Wu, J. Ma, J. Jin, Y. Pi and H. Pang, *Small*, 2024, **20**, 2305548.

28 B. Sun, Y. C. Jiang, Q. L. Hong, X. Liu, F. M. Li, D. S. Li, Y. Yang and Y. Chen, *J. Energy Chem.*, 2023, **85**, 481–489.

29 S. Dai, C. Simms, G. Patriarche, M. Daturi, A. Tissot, T. N. Parac-Vogt and C. Serre, *Nat. Commun.*, 2024, **15**, 3434.

30 S. M. Sohel Rana, O. Faruk, M. Robiul Islam, T. Yasmin, K. Zaman and Z. L. Wang, *Coord. Chem. Rev.*, 2024, **507**, 215741.

31 D. Ji, H. Yang, Q. Zhang, H. Ding, S. Zhang, G. Zhang and H. Pang, *Nano Energy*, 2024, **125**, 109559.

32 A. Purvika, S. Yadav, S. P. Jijoe, T. Tenzin, V. Divya, B. Shahmoradi, K. Wantala, D. Jenkins, G. McKay and H. P. Shivaraju, *Mater. Today Sustainability*, 2024, **26**, 100745.

33 H. Zhu, S. Li, L. Peng, W. Zhong, Q. Wu, S. Cheng and J. Xie, *Nano Energy*, 2024, **125**, 109571.

34 M. Jiang, D. Jiang, X. Cao, J. Wang, Y. Sun, M. Zhang and J. Liu, *Adv. Funct. Mater.*, 2024, **34**, 2312692.

35 D. Ponnalagar, D.-R. Hang, C.-T. Liang and M. M. C. Chou, *Prog. Mater. Sci.*, 2024, **145**, 101308.

36 P. Zhang, S. Raza, Y. Cheng, U. Claudine, A. Hayat, T. Bashir, T. Ali, E. Ghasali and Y. Orooji, *Int. J. Biol. Macromol.*, 2024, **261**, 129146.

37 Z. Pei, H. Tan, J. Gu, L. Lu, X. Zeng, T. Zhang, C. Wang, L. Ding, P. J. Cullen, Z. Chen and S. Zhao, *Nat. Commun.*, 2023, **14**, 818.

38 Z. Hua, H. Song, C. Zhou, Q. Xin, F. Zhou, W. Fan and X. Gao, *Chem. Eng. J.*, 2023, **473**, 145106.

39 J. Zhou, Y. Zhang, M. Zhang, D. Yang, W. Huang, A. Zheng and L. Cao, *Adv. Sci.*, 2024, 2408161.

40 T. Zhou, H. Yuk, F. Hu, J. Wu, F. Tian, H. Roh, Z. Shen, G. Gu, J. Xu, B. Lu and X. Zhao, *Nat. Mater.*, 2023, **22**, 895–902.

41 N. Zhang, X. Zhang, Y. Zhu, D. Wang, W. Liu, D. Chen, R. Li and S. Li, *Int. J. Biol. Macromol.*, 2024, **264**, 130625.

42 Y. Wang, W. Jiang, Y. Yang, C. Wang, D. Zhao, X. Ji, Y. Liu, G. Yang, J. Chen, Y. Ni and G. Lyu, *Energy Storage Mater.*, 2024, **70**, 103483.

43 Y. X. Yu, J. L. Xu, L. W. Zhang, Y. C. Ma and J. M. Luo, *Int. J. Hydrogen Energy*, 2024, **72**, 209–219.

44 H. Zhang, Q. Yang, L. Xu, N. Li, H. Tan, J. Du, M. Yu and J. Xu, *Nano Energy*, 2024, **125**, 109521.

45 X. Li and J. P. Gong, *Nat. Rev. Mater.*, 2024, **9**, 380–398.

46 Y. Fang, X. Xiong, L. Yang, W. Yang, H. Wang, Q. Wu, Q. Liu and J. Cui, *Adv. Funct. Mater.*, 2023, **33**, 2301505.

47 Z. Shan, Y. Yang, H. Shi, J. Zhu, X. Tan, Y. Luan and J. Qin, *Front. Chem.*, 2021, **9**, 755836.

48 M. Safarkhani, A. Aldhaher, E. C. Lima, M. Zargar, E. E. Jung, Y. Huh and N. Rabiee, *ACS Appl. Eng. Mater.*, 2023, **1**, 3080–3098.

49 S. S. Shah, M. A. Aziz, P. I. Rasool, N. Z. K. Mohmand, A. J. Khan, H. Ullah, X. Feng and M. Oyama, *Sustainable Mater. Technol.*, 2024, **39**, e00814.

50 X. Xu, Y. Dong, Q. Hu, N. Si and C. Zhang, *Energy Fuels*, 2024, **38**(9), 7579–7613.

51 M. Downes, C. E. Shuck, B. McBride, J. Busa and Y. Gogotsi, *Nat. Prot.*, 2024, **19**, 1807–1834.

52 D. Wang, C. Zhou, A. S. Filatov, W. Cho, F. Lagunas, M. Wang, S. Vaikuntanathan, C. Liu, R. F. Klie and D. V. Talapin, *Science*, 2023, **379**, 1242–1247.

53 F. Zhou, Q. Xin, Y. Fu, Z. Hua, Y. Dong, M. Ran and X. Gao, *Chem. Eng. J.*, 2023, **464**, 142471.

54 H. Huang, J. Qin, C. Liu, L. Luo, Y. Lan, L. Yang, J. Zhang and H. He, *Carbon*, 2024, **226**, 119171.

55 S. Raza, E. Ghasali, A. Hayat, P. Zhang, Y. Orooji and H. Lin, *Int. J. Biol. Macromol.*, 2024, **254**, 127153.

56 Y. A. Kumar, G. R. Reddy, T. Ramachandran, D. K. Kulurumotlakatla, H. S. Abd-Rabboh, A. A. A. Hafez, S. S. Rao and S. W. Joo, *J. Energy Storage*, 2024, **80**, 110303; H. Zhao, G. Zhao, F. Liu, T. Xiang, J. Zhou and L. Li, *J. Colloid Interface Sci.*, 2024, **666**, 131–140.

57 L. Chen, H. Feng, R. Zhang, S. Wang, X. Zhang, Z. Wei, Y. Zhu, M. Gu and C. Zhao, *ACS Appl. Nano Mater.*, 2020, **3**, 6516–6523.

58 M. Li, H. Zhu, Q. Yuan, T. Li, M. Wang, P. Zhang, Y. Zhao, D. Qin, W. Guo, B. Liu, X. Yang, Y. Liu and Y. Pan, *Adv. Funct. Mater.*, 2023, **33**, 2210867.

59 G. Luo, M. Song, L. An, X. Huang, Q. Zhang, C. Zhang, T. Shen, S. Wang and D. Wang, *J. Energy Chem.*, 2025, **100**, 721–729.

60 K. Deng, Z. Lian, W. Wang, J. Yu, Q. Mao, H. Yu, Z. Wang, L. Wang and H. Wang, *Appl. Catal., B*, 2024, **352**, 124047.

61 Y. Yao, X. Wei, H. Zhou, K. Wei, B. Kui, F. Wu and W. Ye, *ACS Catal.*, 2024, **14**(21), 16205–16213.

62 H. Hao, Y. Lu, N. Liu, W. Bao, F. Sun, C. Zhang, D. Yan and C. Yue, *Fuel*, 2025, **384**, 133981.

63 W. Ye, Y. Zhang, L. Chen, F. Wu, Y. Yao, W. Wang and G. Wang, *Angew. Chem., Int. Ed.*, 2024, **63**, e202410105.

64 Y. A. Kumar, G. R. Reddy, T. Ramachandran, D. K. Kulurumotlakatla, H. S. Abd-Rabboh, A. A. A. Hafez, S. S. Rao and S. W. Joo, *J. Energy Storage*, 2024, **80**, 110303.

65 F. T. Tsai, Y. T. Deng, C. W. Pao, J. L. Chen, J. F. Lee, K. T. Lai and W. F. Liaw, *J. Mater. Chem. A*, 2020, **8**(19), 9939–9950.